

Tailored-Reflectivity Microstructures for Measuring Signal Sensitivity of Optical Coherence Tomography Medical Imaging Systems

Declan M. Fitzgerald, Greta Babakhanova, Christopher M. Stafford, Joshua Guag, Zhuolin Liu, Daniel X. Hammer, Ryan D. Sochol, and Anant Agrawal*

Optical coherence tomography (OCT) is a medical imaging technique that has transformed the practice of ophthalmology via high-resolution visualization and measurement of numerous ocular structures, the retina in particular. Despite its widespread use, the development of tools that help ensure high-quality diagnostic outcomes from OCT systems has not kept pace with the technology's rapid advancements. In this work, a novel microstructure array phantom is presented capable of directly evaluating OCT sensitivity: its ability to distinguish meaningful signal from background noise. Through a combination of two-photon direct laser writing (DLW) and thermally activated selective topographic equilibrium (TASTE), optically smooth microstructures are fabricated and shown to be effective in directly quantifying OCT sensitivity threshold, an advancement over the current practice of extrapolating system sensitivity in the high-signal regime. This phantom serves as proof-of-concept for an easily disseminated regulatory science tool that will increase the consistency of performance reporting anywhere OCT is used. The advanced fabrication techniques used in this study also serve as demonstration of what future retinal phantoms could contain, helping to close the gap between the planar, largely two-dimensional phantoms typically used for OCT systems and the geometrically complex, biomimetic phantoms common to other biomedical imaging modalities.

standard imaging modalities for the human eye, firmly established in ophthalmic research and medical practice.^[4-6] Leveraging low coherence interferometry, OCT operates with time-of-flight optical ranging in an analogous manner to ultrasound by acquiring cross-sectional images from back-reflected light which are then assembled into an image volume.^[7,8] OCT achieves much higher optical spatial resolution than ultrasound imaging, on the scale of 5–15 μm both laterally and axially.^[9] This capability has enabled OCT to be used in a variety of ophthalmic applications, including the diagnosis and management of macular degeneration,^[10-12] and glaucoma.^[13-15] Despite its use in tens of millions of medical scans each year, the creation of tools that could provide greater assurance of high-quality diagnostic outcomes from clinical OCT use has lagged behind OCT's rapid development both in: 1) the absence of precisely-controlled non-planar structures prevalent in the tools of other biomedical imaging systems,

biomimetic or otherwise;^[16,17] and 2) the lack of easily-disseminated test platforms for the evaluation of certain operational metrics.^[18,19] It is an ongoing and well-documented issue that ophthalmic OCT performance can be inconsistent, likely due to this lack of standardization, especially when comparisons are made between devices of different manufacturers.^[20-22]

1. Introduction

Noninvasive in vivo visualization of human organ structural features is an invaluable method for disease diagnosis and management.^[1-3] First invented more than three decades ago, optical coherence tomography (OCT) stands as one of the gold

D. M. Fitzgerald, J. Guag, Z. Liu, D. X. Hammer, A. Agrawal
Center for Devices and Radiological Health
Food and Drug Administration
Silver Spring, MD 20993, USA
E-mail: anant.agrawal@fda.hhs.gov

D. M. Fitzgerald, R. D. Sochol
Department of Mechanical Engineering
University of Maryland
College Park, MD 20742, USA

D. M. Fitzgerald
Department of Mechanical Engineering
University of California
Berkeley, CA 94720, USA

G. Babakhanova
Biosystems and Biomaterials Division
National Institute of Standards and Technology
Gaithersburg, MD 20899, USA

C. M. Stafford
Materials Science and Engineering Division
National Institute of Standards and Technology
Gaithersburg, MD 20899, USA

 The ORCID identification number(s) for the author(s) of this article can be found under <https://doi.org/10.1002/admt.202401959>

DOI: 10.1002/admt.202401959

Sensitivity, a performance metric that defines a system's ability to distinguish between signal and noise in light-starved conditions,^[23] is one such measure that lacks any formal or standardized evaluation technique.

As with any medical technology, proper testing of OCT imaging devices from laboratory development to clinical use is needed to ensure high-quality diagnostic outcomes. One type of physical test object often used with biomedical imaging devices is a phantom, which has carefully established properties for quantifying imaging performance parameters and/or for real-world comparisons between an imaging system's output and known quantities.^[24,25] They are commonplace in medical imaging, with various phantoms having been developed for other 3D imaging modalities such as magnetic resonance imaging (MRI), computerized tomography (CT), and ultrasound.^[26–28] Previous development has demonstrated phantoms for the evaluation of different OCT performance characteristics, including maximum spatial resolution, retinal layer segmentation, and rendering of the foveal pit.^[19,20,29,30] While previous OCT phantoms are effective for their intended purposes, none have yet been successfully applied for the standardization of OCT sensitivity.^[18] We present a new and intuitive approach for OCT sensitivity evaluation by modulating detected signal intensity down to and below the minimum threshold of detectability via a phantom with angled 3D micromirror arrays, emulating the low-light conditions typical during live tissue imaging.

Additive manufacturing (aka 3D printing) technologies are uniquely well suited for the fabrication of 3D structures that require precise geometric control.^[31–33] Many phantoms for biomedical imaging modalities are already developed via additive manufacturing techniques, owing to the rapid prototyping, low cost, and near-limitless geometric versatility of the platforms.^[34–36] However, the need for sub-micrometer feature sizes due to the micrometer-scale resolution of OCT systems means that the majority of extrusion- and vat polymerization-based additive manufacturing techniques are insufficient to produce OCT phantoms.^[37] While traditional mask-based lithographic techniques have more-than-sufficient spatial resolution, they are largely limited to planar structures unfit to fabricate the microstructures needed for this application, leaving two-photon direct laser writing (DLW) as the best alternative.^[38]

DLW uses a femtosecond pulsed IR laser to selectively polymerize a photoresist via two-photon absorption in a point-by-point, layer-by-layer process, building up microstructures with resolutions on the order of 100 nm.^[39–41] This unparalleled combination of resolution and geometric potential has already led to DLW being utilized in many photonics applications, including the fabrication of microlens arrays,^[42] multi-lens objectives,^[43] and waveguide gratings.^[44] Yet, for some optical applications, the inherent surface roughness resulting from the point-by-point curing process can be prohibitive.^[41] While careful selection of voxel path size has shown some success in the reduction of surface roughness,^[45] thermally activated selective topographic equilibrium (TASTE), pioneered by Helmut Schiff's research group, has been demonstrated as a feasible solution for creating an optically smooth surface without significant impact to underlying structures.^[46,47] In order to utilize the TASTE process, the microstructure features must first be printed into a nega-

tive photoresist via two-photon polymerization (Figure 1a,b,g), then transferred into a thermoplastic photoresist, such as poly(methyl methacrylate) (PMMA) (Figure 1c,d). Per TASTE, the PMMA replica of the microstructures is then dosed with vacuum ultraviolet (VUV) light (Figure 1e), and selectively melted, smoothing the surface of the microstructures while maintaining the underlying structure (Figure 1f,h). By pairing DLW and TASTE, we are able to fabricate microstructures with curved surfaces while effectively eliminating the surface roughness inherent to the DLW process. Here we demonstrate the utility of this phantom's tailored reflectivity profile for sensitivity quantification using a state-of-the-art laboratory OCT system for retinal imaging.

2. Results and Discussion

2.1. Phantom Design and Direct Laser Writing

Our design implements microstructures that have slopes ranging from 0 to 18°, for which the effective reflectivity with most OCT systems goes from complete light return to no return at all. To achieve a continuum of slope angles over the desired range, a second-order polynomial defines the reflective surface profile along a single axis. The effective reflectivity is determined both by the refractive index mismatch at the air/device interface, and the angle of the microstructure at any given point. The baseline reflectivity, calculated via $R = [(n_{PMMA} - n_{air}) / (n_{PMMA} + n_{air})]^2$ with $n_{air} = 1$ and $n_{PMMA} = 1.49$, is $R = 0.0387$. The local angle of the microstructure determines the incident light percentage returned to the pupil, assuming Gaussian beam illumination with a $1/e^2$ diameter of 6.7 mm and specular reflection. A first-order optical ray tracing model implemented in MATLAB (MathWorks, Natick, MA) was used to determine the effective reflectivity curve based on device-specific OCT system parameters (Figure 1i).

For the DLW-based printing of the microstructures, a Nanoscribe Photonic GT2 (Nanoscribe GmbH, Germany) was used to print one phantom master, consisting of four microstructures and four scale bars and requiring a total print time of less than 50 min (Figure S1, Supporting Information). Each microstructure was designed to maximize the use of a single print field of the 25× objective resulting in a footprint 250 μm long and 100 μm wide, increasing surface area while preventing additional surface defects due to stitching multiple print fields together. Computer-aided modeling (CAM) simulations and brightfield images of the printing process for a single microstructure can be seen in Figure 2a,b, respectively. Following standard DLW post-processing (see the Experimental Section), each microstructure's integrity was confirmed via scanning electron microscopy (SEM) (Figure 2c). A computer-aided design (CAD) rendering of a complete phantom with all dimensions labeled is provided (Figure S1, Supporting Information). The SolidWorks (Dassault Systèmes, France) design files and Nanoscribe slicing files are also available for download.

2.2. PMMA Feature Transfer and TASTE

A PDMS negative is made of the post-processed DLW print following verification of each microstructure's integrity (Figure 2d;

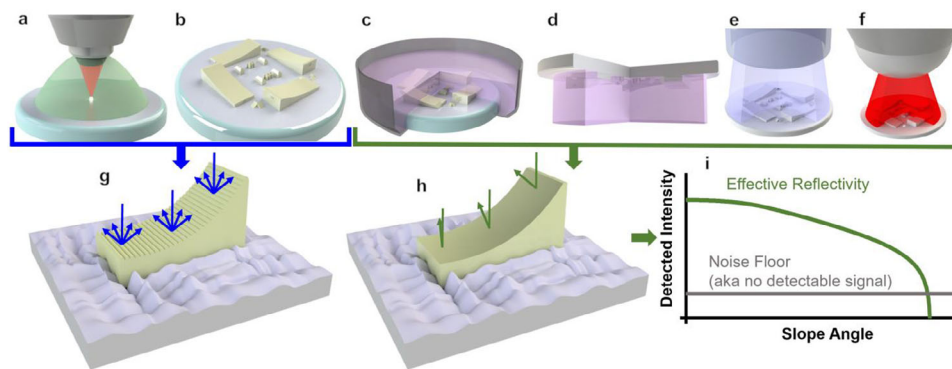


Figure 1. Conceptual illustrations of the direct laser writing (DLW) and subsequent post-processing for the fabrication of optically smooth curved microstructures for the evaluation of ophthalmic optical coherence tomography (OCT) sensitivity. a) A drop of photocurable resist is placed on a substrate and cross-linked via femtosecond pulsed IR laser in a point-by-point, layer-by-layer process. b) The resulting microstructure on the substrate, composed of cured photoresist. Structures not to scale. c) A polydimethylsiloxane (PDMS) negative is created of the print. d) A replica of the print is molded in poly(methyl methacrylate) (PMMA) on top of and fused to a PMMA substrate. e) The PMMA replica is dosed with vacuum-ultraviolet (VUV) light. f) The PMMA replica is heated to selectively melt the top surface of the microstructures. g) Rendering of an individual microstructure with the surface roughness inherent to the DLW process. Substrate texture exaggerated for visual effect. h) Rendering of the same microstructure following post-processing with an optically-smooth surface. i) An effective reflectivity curve via a ray tracing model, demonstrating the predicted change in light return with microstructure slope angle.

Figure S3, Supporting Information). This negative is then used in an elastomeric micromolding process similar to microtransfer molding (μ TM) first demonstrated by Whitesides' group.^[48] The thermoplastic photoresist PMMA is dissolved in solvent anisole and pipetted atop the overturned PDMS negative. The PMMA/anisole solution is allowed to partially harden on a hotplate prior to the placement of the PMMA substrate atop them, to ensure all air pockets are purged (Figure S3, Supporting Information). The PMMA substrate is then placed atop the negative and weighted to ensure conformal contact (Figure 2e). The PDMS negative is then peeled away once all anisole has evaporated. Using PMMA as both the thin film and substrate in this elastomeric micromolding process serve two purposes: 1) it increases the interface strength between the molded microstructures and the substrate, a known fail-

ure point with μ TM,^[49] and 2) it minimizes the reflection from the substrate/microstructure interface by matching the refractive indices as closely as possible. Bright reflections resulting from a large refractive index mismatch between the substrate and thin film will saturate OCT volumes, preventing accurate intensity readings. The molding process was used to produce four faithful replicas of the original DLW print, which accurately reproduced both macroscopic structural features and sub-micrometer features such as individual slicing layers (Figure 3a,c).

The surface texture resulting from DLW's point-by-point curing process, transferred into the PMMA replica, prevents the microstructures from acting as perfect mirrors. As is necessary for TASTE, PMMA's positive-tone photoresist mechanism relies on the absorption of sufficient energy to cause significant rates

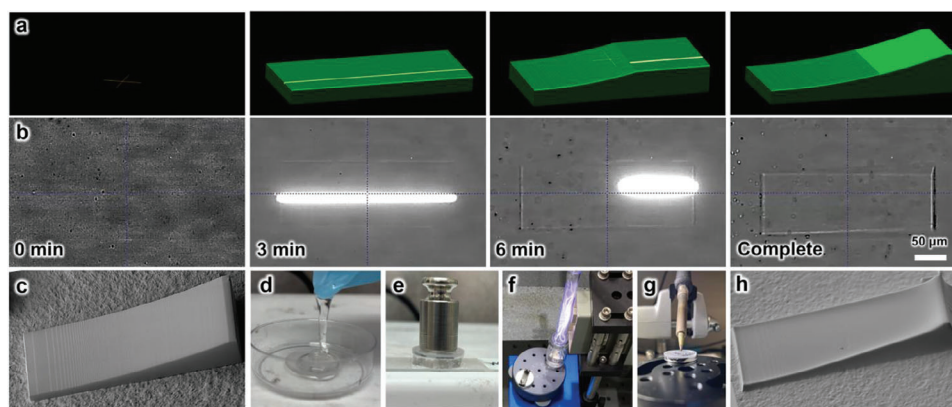


Figure 2. Fabrication procedure for the combined DLW-based printing and thermally activated selective topographic equilibrium (TASTE) for the fabrication of OCT sensitivity phantoms. a,b) the DLW approach for printing variably-sloped microstructures, with a) computer-aided manufacturing (CAM) simulations, and b) corresponding brightfield images of the printing process. c) Scanning electron microscopy (SEM) image of a single variably-sloped microstructure verifying print success. d) PDMS mold creation of the post-processed DLW print. e) A replica of the mold is formed via a PMMA/anisole solution and prefabricated PMMA substrate. f) The PMMA replica is dosed with VUV light via xenon lamp. g) The posed PMMA replica is selectively heated via a mounted soldering iron. h) SEM image of a post-processed microstructure.

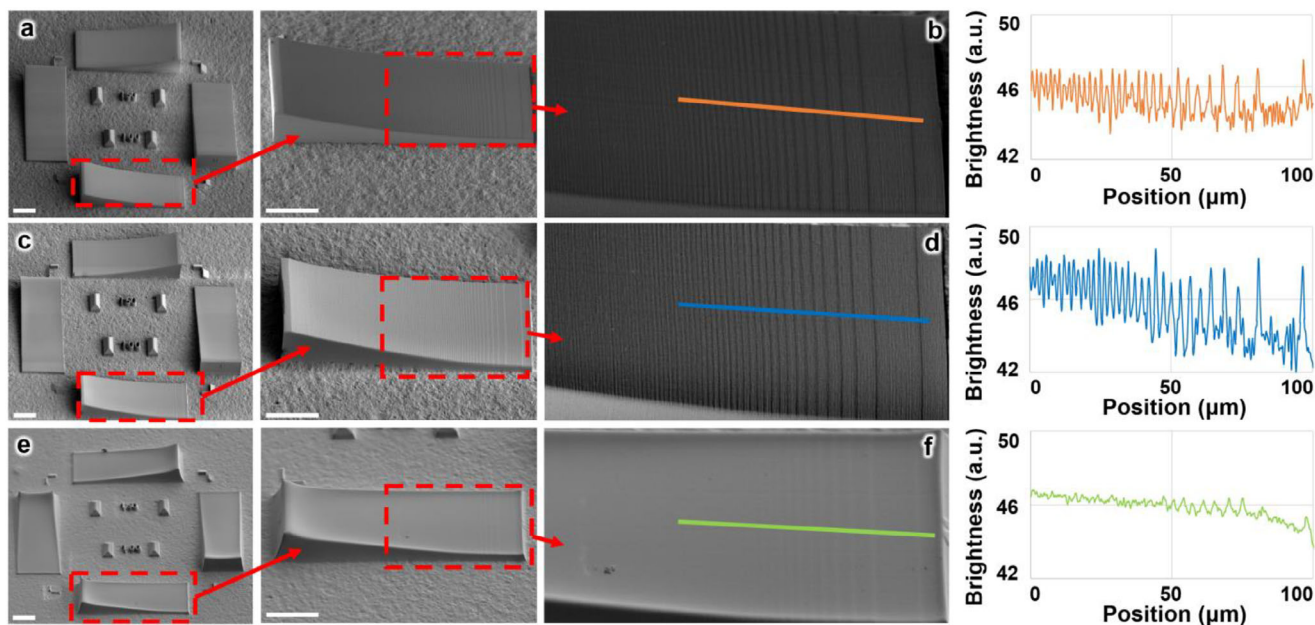


Figure 3. Fabrication results for a,b) the DLW-based printing, c,d) the elastomeric micromolding replication, and e,f) the TASTE-based post-processing. All scale bars = 50 μm . SEM images of the entire phantom, a single microstructure, and a close-up view of a single microstructure are seen from left to right respectively, for a) the printed microstructure array, c) the PMMA replica, and e) the post-processed phantom. Image brightness profile plots for the corresponding close-up microstructure views can be seen for b) the printed microstructure array, d) the PMMA replica, and f) the post-processed phantom.

of main chain scission and side group removal, decreasing average molecular weight.^[50-53] This overall reduction in average molecular weight decreases the glass transition temperature and melting point of the polymer.^[54] By irradiating PMMA with VUV light (Figure 2f), we can isolate this reduction in transition temperature to a superficial 1 μm thick layer of the material, causing the surface texture to melt (Figure 2g) at reduced temperatures while leaving the underlying structural PMMA unchanged (Figure 2h).^[47]

SEM provides visual evidence that the TASTE process effectively reduced the surface texture resulting from the DLW print process. The prominent stair-like features, seen both in the IP-Dip2 print (Figure 3a,b) and the PMMA replica (Figure 3c,d), become less obtrusive on the post-processed phantom (Figure 3e,f), as further supported by AFM measurements (Figure S2, Supporting Information). The reflow process also resulted in slight structural changes, altering the slope profile of the angled microstructures across both their width and length (Figure 4). Compared to the original print (Figure 4a–c), the processed phantom developed a cupped surface across its width, with the prominence of the sloped edges increasing with height (Figure 4d–f). Additionally, in contrast to the linear slope profile observed in the DLW print (Figure 4c), the reflowed PMMA exhibits a much steeper slope at the tallest region of the angled element (Figure 4f). This then quickly tapers to a more linear, shallow slope for the remainder of the structure's length. This results in a longer section of the microstructure having a lower-sloped, more highly reflective surface, which then quickly transitions to a steeper-sloped region for the remaining length of the microstructure.

2.3. Quantitative Reflow Evaluation

The OCT device used for the initial post-processing evaluation is an ophthalmic spectral-domain adaptive optics (AO)-enhanced OCT (AO-OCT) system constructed at the FDA.^[55] As an ophthalmic imaging system, it relies on refraction by the cornea and crystalline lens of the human eye to image the retina. To mimic this behavior, the phantom is loaded into a custom-built model eye with an achromatic lens matching the dioptric power of a human eye. Adaptive optics, a technology first used by astronomers to correct for atmospheric turbulence that perturbed ground-based telescopes,^[56] has since been adapted to correct for ocular aberrations that result from light passing through the anterior segment of the human eye.^[57] The system relies on a wavefront sensor to detect the aberrations and a deformable mirror to correct the wavefront error.^[58] The textured surface of the glass diffuser on which the original design is printed has two critical functions: 1) The diffuse reflection provides a more uniform wavefront sensor signal, providing better AO correction; 2) It reduces the overall reflectivity from the areas around the microstructures, preventing detector saturation. Adaptive optics is used to improve the lateral resolution of the OCT system but has little impact on how our phantom evaluates system sensitivity, which is the target of this work.

High-magnification AO-OCT scans (1.66 pixels μm^{-1}) were taken of the four microstructures on each of the four phantoms, for a total of sixteen variable-sloped micromirrors (Figure 5). Additional scans were taken of the DLW-printed microstructures for post-processing efficacy evaluation. The volumes were loaded into ImageJ (NIH, Bethesda, MD), where dimensions were

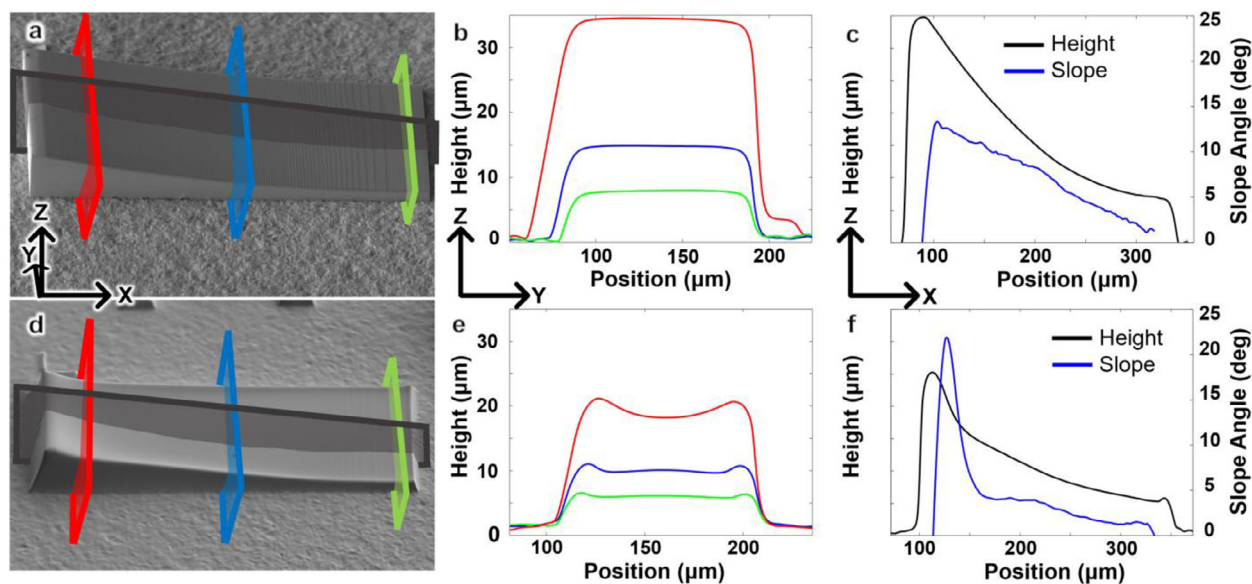


Figure 4. An SEM image and quantitative surface profile plots of a single microstructure from a–c) the printed microstructure array and d–f) the post-processed phantom determined via stylus profilometry. a) An SEM image of a single DLW-printed microstructure with red, blue, and green vertical cross-section indicators and a black horizontal cross-section indicator. b) The surface profile across the width of the microstructure at sequentially decreasing heights indicated in red, blue, and green. c) Both the surface profile of the microstructure along its length, indicated in black, and the absolute value of an instantaneous slope profile of the microstructure along its length, indicated in blue. d) An SEM image of a single post-processed phantom microstructure with red, blue, and green vertical cross-section indicators and a black horizontal cross-section indicator. e) The surface profile across the width of the microstructure at sequentially decreasing heights indicated in red, blue, and green. f) Both the surface profile of the microstructure along its length, indicated in black, and the absolute value of an instantaneous slope profile of the microstructure along its length, indicated in blue.

calibrated via scale-bar separation. Scale bar separation was confirmed via brightfield microscopy (Optiphot, Nikon, Tokyo). Once properly scaled, the OCT scans were compared to the stylus profilometry (Dektak 150, Veeco, New York) map of the true surface profiles to get a pixel-by-pixel mapping between OCT intensity and phantom slope angle, allowing for a true evaluation of detected signal intensity versus microstructure surface reflectivity.

This analysis serves as an application-driven assessment of the change in microstructure reflectivity that resulted from the TASTE post-processing procedure. An unpaired *t*-test found that the detected intensity is not significantly different between the print and the processed phantoms for slope angles less than 12° ($p > 0.05$, $N = 84$) but is significantly lower for the processed phantom for slope angles greater than 12° ($p < 0.001$, $N = 164$) (Figure 5b,e). A significantly lower detected intensity at higher slope angles indicates that the microstructure's surface has become more optically smooth, causing it to reflect the majority of the incident beam away from the detector as intended. For further verification, atomic force microscopy (AFM) measurements were taken across the surface of both a reflowed phantom and the original DLW print. The average root mean squared (RMS) roughness of the reflowed phantom and DLW print were 6.2 and 19.2 nm respectively, taken across $400 \mu\text{m}^2$ footprints at the base of two angled elements on each sample. This demonstrates a $\approx 68\%$ overall decrease in surface roughness, though the DLW print had some additional fine roughness (± 5 nm) from a gold sputter coating layer, while the reflowed phantom was unmodified (Figure S2, Supporting Information). The OCT measurements confirm that the surface roughness inherent to the DLW process limits the optical performance of the print, as an-

ticipated by previous work.^[41,45] The stair-like geometry allows the local flat spots of each individually printed layer to reflect light back to the detector, despite the intended slope of the region (Figure 5a–c). The OCT and AFM measurements verify that the processed phantom has had these flat spots reflowed into a continuous curve, successfully preventing the sporadic return of light in higher-sloped regions (Figure 5d–f).

2.4. OCT Sensitivity Analysis

The sensitivity analysis was performed on two OCT devices: 1) the AO-OCT system described in the previous section, using the same data employed in the post-processing efficacy evaluation, and 2) a commercially available OCT system without AO (GAN610C1, Thorlabs, Newton, NJ). This analysis serves to assess the phantom's ability to determine an OCT system's minimum reflectivity (R_{min}) threshold. For the phantom to directly quantify the OCT minimum detectable reflectivity threshold, it had to both: 1) achieve surface conditions for which the returned signal drops down to the noise floor, and 2) allow for accurate estimation of the effective reflectivity of the microstructure at the location where this condition is achieved. The phantom was able to reach the noise floor threshold across multiple samples in a repeatable manner for both systems (Figure 5e,g). Additionally, by using stylus profilometry to confirm precise surface slope angles despite structural changes during reflow, the phantom's effective reflectivity for the OCT system is known for each place the noise floor was reached. By taking a 10-point moving average of the data and determining the effective reflectance of the slope angle where

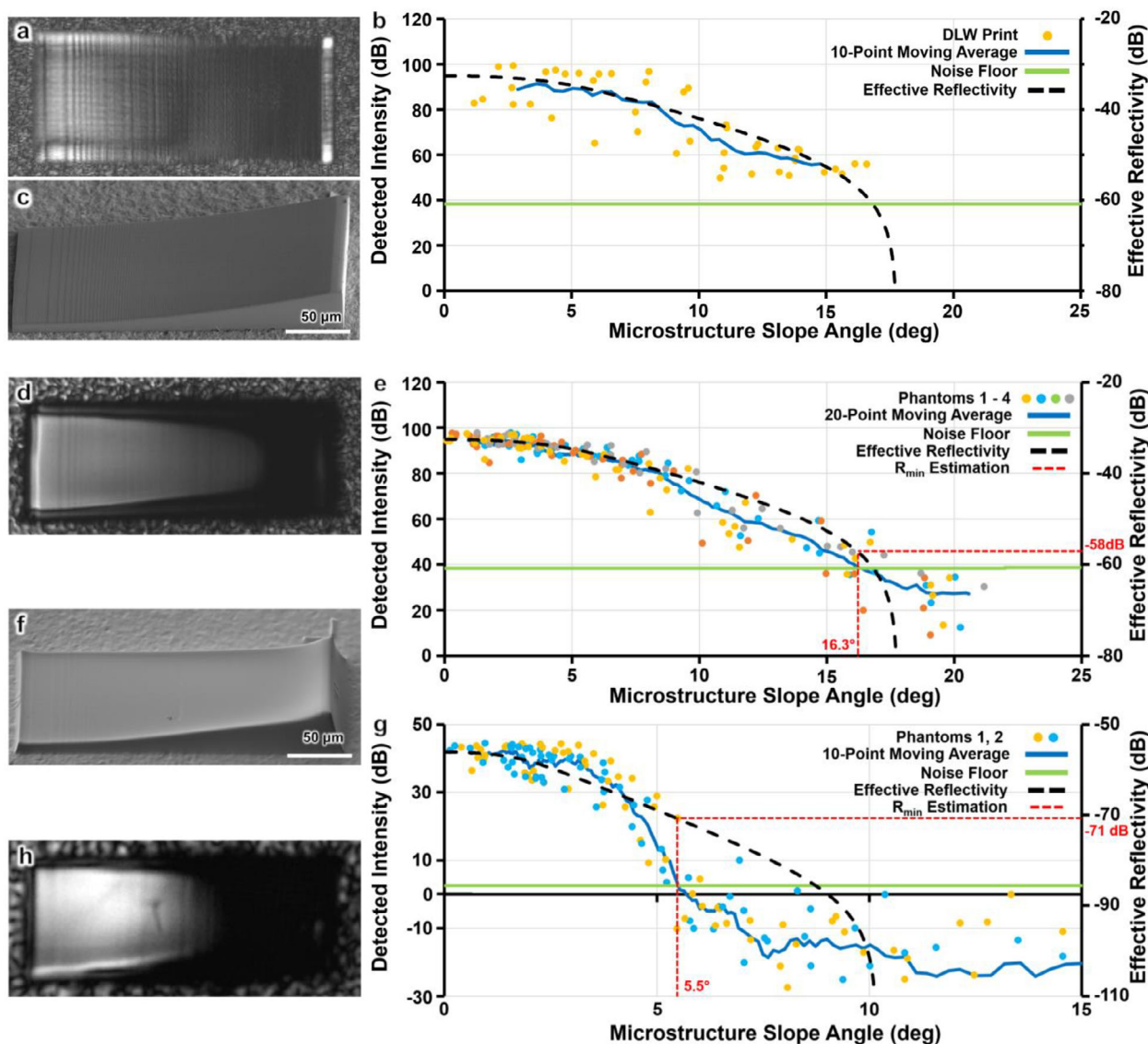


Figure 5. Experimental results for OCT evaluation of post-processing and the analysis of OCT sensitivity. a) AO-OCT image of a single DLW-printed microstructure, with a maximum-intensity projection performed over the entire image volume. Maximum-intensity projection serves to ensure that the pictured brightness results from the most reflective point in the volume: the air/PMMA interface at the phantom surface. b) Detected intensity versus slope angle for the DLW-printed microstructure with a 10-point moving average. The effective reflectivity of a smooth surface for each slope angle is plotted on the second vertical axis. c) SEM image of the DLW-printed microstructure, providing orientation reference for AO-OCT image. d) AO-OCT image of a single processed phantom microstructure, again with a maximum-intensity projection. e) AO-OCT detected intensity versus slope angle for the four phantoms with a 20-point moving average to account for a larger dataset size. The effective reflectivity of a smooth surface for each slope angle is plotted on the second vertical axis. The intersection of the experimental minimum reflectivity (R_{\min}) threshold with the effective reflectivity curve is highlighted in red. f) SEM image of the processed microstructure for reference. g,h) detected intensity versus slope angle plot and commercial OCT image of representative angled element, respectively.

the intensity values crossed the noise floor, we can determine the OCT system's sensitivity. With a threshold angle of 16.3° , we find R_{\min} to equal -58 dB for the AO-OCT system. The commercial OCT system produced a threshold angle of 5.5° for a corresponding R_{\min} of -71 dB. The higher sensitivity of the commercial system is expected, as the incorporation of AO-enabling optical elements diminishes light returned to the detector, though other system factors also contribute to the relative sensitivity values.

The non-phantom-based traditional method of OCT sensitivity evaluation uses the maximum signal-to-noise ratio (SNR) a device can achieve, determined by imaging a highly reflective surface to maximize I_{sample} , where $\text{SNR} = \frac{I_{\text{sample}}^2}{\sigma_{\text{background}}^2}$ and $\text{SNR}_{\max} = -R_{\min}$.^[18,59] In our previous work we have noted that this method for evaluating system sensitivity is limited by an assumed linear relationship between performance in light-abundant and light-starved conditions, likely making it unreliable.^[18] Just as the

minimally reflective sloped regions of the microstructures enable a direct calculation of R_{\min} , the highly reflective flat regions enable a direct calculation of SNR_{\max} . This provides a means to explicitly compare sensitivity assessment methods. By averaging the SNR values of the data points closest to a slope angle of zero, where the signal return is the highest, we found $SNR_{\max} = 90$ dB for the AO-OCT system. This result is 7 dB higher than Liu et al. reported for the same system, a difference likely due to this study using a slower scan speed with longer exposure time for each pixel and a shorter focal length model eye with a higher numerical aperture (NA).^[55] These same calculations produce $SNR_{\max} = 95$ dB for the commercial device. This result is within the user manual-reported scan speed-dependent sensitivity range of 84–102 dB for this system.

This result of SNR_{\max} for the AO-OCT system is 32 dB higher than the value determined via direct measurement of R_{\min} . In previous work, we also directly measured R_{\min} via microsphere suspensions with known reflectivities and found that it similarly underestimated the traditional SNR_{\max} calculation by 26 dB.^[18] While there is no microsphere suspension measurement of R_{\min} for the commercial system, the comparison between R_{\min} and SNR_{\max} from this phantom produces a disparity of 24 dB, indicating a consistent method difference across different types of OCT devices. The approximate concordance between our previous and current results highlights the fact that any assumed linear relationship between OCT system performance in light-abundant (i.e., under a shot noise-limited condition) and light-starved conditions is not valid and that the widely used sensitivity analysis procedure vastly overestimates system performance. Unlike our previous concept for sensitivity phantoms, which had discrete reflectivities in a liquid form, the phantom presented in this work has a continuous range of reflectivities in a solid-state device, providing a long shelf life and the ability to evaluate a variety of OCT systems without modification.

3. Conclusion

The noninvasive in vivo visualization of retinal structures is invaluable to ophthalmic disease diagnosis and management.^[60,61] OCT serves as one of the primary biomedical imaging platforms for this purpose, with applications ranging from biomarker tracking to the guiding of surgical interventions.^[62] Despite its critical role in ophthalmic medicine, the library of tools available for the verification and assurance of high-quality OCT performance has lagged behind.^[17,18] In this work we developed an optical phantom for direct OCT sensitivity evaluation with optically smooth curved micromirror arrays fabricated via combining the microfabrication geometric versatility of DLW and the selective surface smoothing of TASTE and demonstrated with a state-of-the-art laboratory retinal OCT system.

As the original microstructure design leverages two-photon polymerization-based DLW, the geometric versatility of the microstructures is high on limitless. This versatility makes possible the development of a variety of other phantom types with little modification to the manufacturing process described in this work. Such phantoms could include those for the evaluation of lateral resolution or dynamic range. While likely requiring different post-processing than used in this work, DLW could also be used to fabricate biomimetic phantoms, such as those

representing individual photoreceptor cells in the retina or the choroidal microvasculature within and below the retina. DLW's utility has already been thoroughly demonstrated for microfluidic applications,^[63–65] with Horng et al. demonstrating a retinal vasculature phantom for fluorescence microscopy.^[66]

The promising thermal reflow results were largely consistent with the previous works from Helmut Schiff's group, though slightly larger structural changes were observed.^[46,47] While the subtle difference in result has not yet been reconciled, the dissimilarity may result from the inconsistent PMMA molding techniques, the VUV irradiation equipment, or the thermal exposure process, among other potential sources. Further investigation into alternative or additional reflow processes, such as solvent-vapor-induced reflow,^[67] may serve to diminish the observed macroscopic structural changes or further reduce surface roughness. The utility of this depth-confined surface smoothing procedure has potential applications across many fields, with particular utility in optics. Two photonic applications for which carefully tuned curved micromirror arrays, as we have demonstrated in this work, are currently being investigated include beam coupling^[68] and atomic clocks.^[69]

We anticipate that this OCT phantom will help remedy the ongoing inconsistency issues known to afflict OCT systems. The phantom's solid-state composition, continuous range of reflectivities, and easily replicated nature are key features that enhance its stability and ease of use for OCT device development, deployment, and maintenance. Future work on this device could optimize the dimensions of each microstructure for interchangeable use on a wide range of OCT systems, ensuring compatibility with the majority of currently deployed devices. Nevertheless, this phantom has shown to be an effective tool for OCT sensitivity evaluation, supporting greater harmonization and reduced variability related to OCT device use.

4. Experimental Section

Phantom Printing via DLW: The microstructures—modeled using SolidWorks (Dassault Systèmes, France)—were designed with a footprint of $250 \mu\text{m} \times 100 \mu\text{m}$, optimized to maximize surface area within the constraints of a single print field. The microstructures were arranged in a set of four with the primary slopes pointing in each cardinal direction. The second-order polynomial function defining the surface profile was $0.000683x^2$, with x referring to the distance in μm along the long axis of the microstructure. Two pairs of scale bars were placed in the center, with separations of 100 and 150 μm . The layout was exported as an STL and uploaded to the CAM software, DeScribe (Nanoscribe). Slicing and hatching parameters were set to 100 nm to minimize initial surface texture. The 1200-grit sand-blasted glass diffuser (DG1200, Thorlabs, Newton, NJ) was exposed to oxygen plasma for 30 min prior to a 2-h bath in ethanol (50 mL) and 3-(trimethoxysilyl)propyl methacrylate (250 μL) for improved adhesion. The substrate was then rinsed with isopropanol (IPA) and blow-dried with nitrogen. A drop of photoresist IP-Dip2 (Nanoscribe) was placed on the substrate, which was then loaded into the Nanoscribe Photonic Professional GT2 DLW 3D printer. Dip-in laser lithography (DiLL) mode was used with the 25 \times objective lens, a laser power of 20 mW, and a laser scanning speed of 40 000 $\mu\text{m s}^{-1}$. The completed print was soaked in a propylene glycol methyl ether acetate (PGMEA) bath for 15 min, followed by an isopropyl alcohol (IPA) bath for 5 min, and finally placed in a UV cure box for 10 min.

PMMA Replication: The post-processed glass substrate was placed print side up in a plastic petri dish covered with polydimethylsiloxane (PDMS) elastomer (Sylgard 182, Dow Corning) and cured for 6 h on a

hotplate at 65 °C. Once solidified, the PDMS and substrate were removed from the petri dish. The substrate was then carefully peeled out of the PDMS negative, ensuring no lateral movement between the print and the PDMS mold while in contact. A circle was cut in the PDMS to remove the region that was in conformal contact with the print and glass surface, creating a stamp-like PDMS negative of the print. A 5:1 by-mass solution of anisole and 120k molecular weight poly(methyl methacrylate) (PMMA) (both from Sigma–Aldrich, Saint Louis, MO) was premixed in a glass beaker. The PDMS negative was placed on a hot plate at 65 °C, and 30 μL of the anisole/PMMA solution was placed on the surface of the PDMS, fully covering the region with the print. This was left for 5 min to purge any remaining bubbles. A 25-mm diameter PMMA disk (19-634, Edmund Optics, Barrington, NJ) was then placed on top of the PDMS negative and secured with a 35-g weight, remaining on the hotplate for another 20 min. The PMMA disk was then peeled away from the PDMS negative, taking the newly cured PMMA film with it.

TASTE: A vacuum ultraviolet (VUV) xenon lamp (LC-X, Ophos Instrument Company, Maryland) centered at a wavelength of $\lambda = 172$ nm was used to irradiate the PMMA film. The lamp was ignited via a tesla coil and ignition was maintained with a microwave emitter. Each PMMA sample was exposed to a total VUV dose of 1.458 J cm^{-2} , with an estimated 50% absorbed within the first micron of the PMMA film. A mounted soldering iron was used to heat the surface of the substrate containing the microstructure array. A thermocouple was used to confirm PMMA surface temperature. A surface temperature of 87 ± 1.5 °C was maintained for 2.5 min to complete the reflow process.

Phantom Characterization: Low accelerating-voltage SEM images (Mira 3, TESCAN, Brno-Kohoutovice, Czech Republic) were taken of 5 nm gold-coated sacrificial samples under vacuum to provide high-resolution images of the phantom at every stage of its development. SEM images were also taken of the phantoms without the gold coating to verify integrity. Stylus profilometry (Dektak 150, Veeco, New York, USA) was performed with a 12.5 μm tip diameter to create a topographical map of each microstructure for determination of true slope values and evaluate structural changes post-reflow. Brightfield microscopy (Optiphot, Nikon, Tokyo, Japan) was used to confirm scale bar separation and verify microstructure footprint post-reflow, which was then used to establish scale within each OCT image. AFM imaging was performed on a Bruker Dimension Icon AFM operating in tapping mode. Images were collected using RTESPA-300 probes (Bruker Nano) with a nominal spring constant of 40 N m^{-1} and a nominal radius of curvature of 8 nm. The samples were imaged at a scan rate of 0.5 Hz over an area of $20 \mu\text{m} \times 20 \mu\text{m}$. The fast scan axis was always oriented parallel to the long side of the angled element. AFM image analysis was performed using both Bruker NanoScope Analysis and Gwyddion software packages, and images were flattened prior to performing section analysis and roughness calculations.

OCT Imaging and Evaluation: For AO-OCT data collection, each phantom was placed in the back of a model eye with a single lens (49-952-INK, Edmund Optics) mimicking the total refraction of the human eye to enable the OCT system to image the phantom as it would a human retina. This model eye was then mounted on the chinrest of the OCT system to minimize vibration. AO-OCT scans ($1.66 \text{ pixels } \mu\text{m}^{-1}$) were taken of each phantom's microstructures, with additional scans taken of the DLW-printed microstructures. For data collection from the commercial OCT device, the phantoms were placed on a flat surface directly underneath the objective, which was translated vertically to bring the phantom into focus. OCT scans ($1.0 \text{ pixels } \mu\text{m}^{-1}$) were taken of each angled element of two phantoms. With both systems, a neutral density filter was inserted in the OCT sample arm light path to prevent detector saturation (nominal optical density 1.0 for AO-OCT, and 3.0 for commercial OCT).

These 32-bit floating-point OCT volumes were then loaded into ImageJ (NIH, Bethesda, MD) where ROIs were overlaid to establish a scale for the mapping of OCT intensity values to profilometer slope angles. Intensity versus slope angle was plotted collectively for the fifteen microstructures imaged with the AO-OCT system, as well as for the eight imaged via the commercial OCT system. A separate plot for the AO-OCT imaging of the four microstructures of the original DLW-printed sample was also shown. The noise floor was established by taking the standard deviation of the

reported signal intensity from a volume of the OCT scan that corresponded to open air. The noise floor was averaged over every phantom imaged by each system and was measured separately for the DLW-printed sample.

Statistical Analysis: Statistical significance was determined via an unpaired *t*-test. One-tailed *p* values of greater than 0.05 were considered statistically indistinguishable, with no fewer than 10 samples in any group.

Supporting Information

Supporting Information is available from the Wiley Online Library or from the author.

Acknowledgements

The authors gratefully acknowledge the assistance of Gillian Nave, formerly of the National Institute of Standards and Technology, for assistance with spectral irradiance measurements of the VUV lamp. This research was supported in part by U.S. National Science Foundation (NSF) Award #1943356. Declan M. Fitzgerald was supported in part by the Oak Ridge Institute for Science and Engineering (ORISE) fellowship program at the FDA.

The mention of commercial products, their sources, or their use in connection with material reported herein is not to be construed as either an actual or implied endorsement of such products by the Department of Health and Human Services. Certain equipment, instruments, software, or materials are identified in this paper in order to specify the experimental procedure adequately. Such identification is not intended to imply recommendation or endorsement of any product or service by NIST, nor is it intended to imply that the materials or equipment identified are necessarily the best available for the purpose. Official contribution of the National Institute of Standards and Technology; not subject to copyright in the United States.

Conflict of Interest

The authors declare no conflict of interest.

Data Availability Statement

The data that support the findings of this study are available from the corresponding author upon reasonable request.

Keywords

3D Printing, additive manufacturing, direct laser writing, ophthalmic imaging, optical coherence tomography, signal sensitivity

Received: November 22, 2024

Revised: April 30, 2025

Published online:

- [1] F. Mazzoni, C. Müller, J. DeAssis, D. Lew, W. M. Leevy, S. C. Finemann, *Sci. Rep.* **2019**, *9*, 1590.
- [2] R. K. Meleppat, K. E. Ronning, S. J. Karlen, M. E. Burns, E. N. Pugh, R. J. Zawadzki, *Sci. Rep.* **2021**, *11*, 16252.
- [3] X. Hadoux, F. Hui, J. K. H. Lim, C. L. Masters, A. Pébay, S. Chevalier, J. Ha, S. Loi, C. J. Fowler, C. Rowe, V. L. Villemagne, E. N. Taylor, C. Fluke, J.-P. Soucy, F. Lesage, J.-P. Sylvestre, P. Rosa-Neto, S. Mathotaarachchi, S. Gauthier, Z. S. Nasreddine, J. D. Arbour, M.-A. Rhéaume, S. Beaulieu, M. Dirani, C. T. O. Nguyen, B. V. Bui, R. Williamson, J. G. Crowston, P. van Wijngaarden, *Nat. Commun.* **2019**, *10*, 4227.

- [4] R. Chopra, S. K. Wagner, P. A. Keane, *Eye* **2021**, 35, 236.
- [5] N. Minakaran, E. R. de Carvalho, A. Petzold, S. H. Wong, *Eye* **2021**, 35, 17.
- [6] S. Aumann, S. Donner, J. Fischer, F. Müller, *High Resolution Imaging in Microscopy and Ophthalmology*, Springer, Berlin NY, **2019**, pp. 58–85.
- [7] J. G. Fujimoto, C. Pitris, S. A. Boppart, M. E. Brezinski, *Neoplasia* **2000**, 2, 9.
- [8] D. Huang, E. A. Swanson, C. P. Lin, J. S. Schuman, W. G. Stinson, W. Chang, M. R. Hee, T. Flotte, K. Gregory, C. A. Puliafito, J. G. Fujimoto, *Science* **1991**, 254, 1178.
- [9] D. R. Williams, *Vision Res.* **2011**, 51, 1379.
- [10] C. V. Regatieri, L. Branchini, J. S. Duker, *Ophthalmic Surg. Lasers Imaging* **2011**, 42, S56.
- [11] P. A. Keane, P. J. Patel, S. Liakopoulos, F. M. Heussen, S. R. Sadda, A. Tufail, *Surv. Ophthalmol.* **2012**, 57, 389.
- [12] L. de Sisternes, N. Simon, R. Tibshirani, T. Leng, D. L. Rubin, *Invest Ophthalmol. Vis. Sci.* **2014**, 55, 7093.
- [13] D. WuDunn, H. L. Takusagawa, A. J. Sit, J. A. Rosdahl, S. Radhakrishnan, A. Hogue, Y. Han, T. C. Chen, *Ophthalmology* **2021**, 128, 1222.
- [14] D. S. Grewal, A. P. Tanna, *Curr. Opin. Ophthalmol.* **2013**, 24, 150.
- [15] T. C. Chen, A. Hogue, A. K. Junk, K. Nouri-Mahdavi, S. Radhakrishnan, H. L. Takusagawa, P. P. Chen, *Ophthalmology* **2018**, 125, 1817.
- [16] G. Lamouche, B. F. Kennedy, K. M. Kennedy, C.-E. Bisaillon, A. Curatolo, G. Campbell, V. Pazos, D. D. Sampson, *Biomed. Opt. Express* **2012**, 3, 1381.
- [17] T. Heikka, G. Ometto, G. Montesano, S. Rowe, N. M. Jansonius, D. P. Crabb, *Biomed. Opt. Express* **2020**, 11, 1306.
- [18] A. Agrawal, T. J. Pfefer, P. D. Woolliams, P. H. Tomlins, G. Nehmetallah, *Biomed. Opt. Express* **2017**, 8, 902.
- [19] J. Baxi, W. Calhoun, Y. J. Sepah, D. X. Hammer, I. Ilev, T. Joshua Pfefer, Q. D. Nguyen, A. Agrawal, *J Biomed. Opt.* **2014**, 19, 021106.
- [20] R. De Kinkelder, D. M. de Bruin, F. D. Verbraak, T. G. van Leeuwen, D. J. Faber, *J Biophotonics* **2013**, 6, 314.
- [21] A. Agrawal, J. Baxi, W. Calhoun, C. L. Chen, H. Ishikawa, J. S. Schuman, G. Wollstein, D. X. Hammer, *Invest Ophthalmol. Vis. Sci.* **2016**, 57, OCT413.
- [22] L. Pierro, M. Gagliardi, L. Iuliano, A. Ambrosi, F. Bandello, *Invest Ophthalmol. Vis. Sci.* **2012**, 53, 5912.
- [23] Z. Yaqoob, J. Wu, C. Yang, *BioTechniques* **2005**, 39, 6.
- [24] J. Jung, S. Y. Song, S. M. Yoon, J. Kwak, K. Yoon, W. Choi, S. Y. Jeong, E. K. Choi, B. Cho, *Int. J. Radiat. Oncol. Biol. Phys.* **2015**, 92, 745.
- [25] D. Wallace, J. A. Ng, P. J. Keall, R. T. O'Brien, P. R. Poulsen, P. Juneja, J. T. Booth, *Phys. Med. Biol.* **2015**, 60, 4835.
- [26] E. Villa, N. Arteaga-Marrero, J. González-Fernández, J. Ruiz-Alzola, J. Gonzalez Fernandez, *Sci. Rep.* **2020**, 10, 20401.
- [27] A. Valladares, T. Beyer, I. Rausch, *Med. Phys.* **2020**, 47, 2023.
- [28] K. E. Keenan, M. Ainslie, A. J. Barker, M. A. Boss, K. M. Cecil, C. Charles, T. L. Chenevert, L. Clarke, J. L. Evelhoch, P. Finn, D. Gembris, J. L. Gunter, D. L. G. Hill, C. R. Jack, E. F. Jackson, G. Liu, S. E. Russek, S. D. Sharma, M. Steckner, K. F. Stupic, J. D. Trzasko, C. Yuan, J. Zheng, *Magn. Reson. Med.* **2018**, 79, 48.
- [29] A. Agrawal, C. W. Chen, J. Baxi, Y. Chen, T. J. Pfefer, *Biomed. Opt. Express* **2013**, 4, 1166.
- [30] A. Agrawal, T. J. Pfefer, N. Gilani, R. Drezek, *Opt. Lett.* **2010**, 35, 2269.
- [31] J. D. Hubbard, R. Acevedo, K. M. Edwards, A. T. Alsharhan, Z. Wen, J. Landry, K. Wang, S. Schaffer, R. D. Sochol, *Sci. Adv.* **2021**, 7, 5257.
- [32] H. Cui, D. Yao, R. Hensleigh, H. Lu, A. Calderon, Z. Xu, S. Davaria, Z. Wang, P. Mercier, P. Tarazaga, X. R. Zheng, *Science* **2022**, 376, 1287.
- [33] S. Sarker, A. Colton, Z. Wen, X. Xu, M. Erdi, A. Jones, P. Kofinas, E. Tubaldi, P. Walczak, M. Janowski, Y. Liang, R. D. Sochol, *Adv. Mater. Technol.* **2023**, 8, 2201641.
- [34] M. F. Bieniosek, B. J. Lee, C. S. Levin, *Med. Phys.* **2015**, 42, 5913.
- [35] R. Tino, A. Yeo, M. Leary, M. Brandt, T. Kron, *Technol. Cancer Res. Treat.* **2019**, 18, 1.
- [36] V. Filippou, C. Tsoumpas, *Med. Phys.* **2018**, 45, 740.
- [37] L. Y. Zhou, J. Fu, Y. He, *Adv. Funct. Mater.* **2020**, 30, 2000187.
- [38] M. Malinauskas, M. Farsari, A. Piskarskas, S. Juodkazis, *Phys. Rep.* **2013**, 533, 1.
- [39] L. Yang, F. Mayer, U. H. F. Bunz, E. Blasco, M. Wegener, *Light: Adv. Manuf.* **2021**, 2, 17.
- [40] A. C. Lamont, M. A. Restaino, M. J. Kim, R. D. Sochol, *Lab Chip* **2019**, 19, 2340.
- [41] X. Zhou, Y. Hou, J. Lin, *AIP Adv.* **2015**, 5, 030701.
- [42] N. Tsutsumi, J. Hirota, K. Kinashi, W. Sakai, *Opt. Express.* **2017**, 25, 31539.
- [43] T. Gissibl, S. Thiele, A. Herkommer, H. Giessen, *Nat. Photonics* **2016**, 10, 554.
- [44] N. Tsutsumi, K. Kaida, K. Kinashi, W. Sakai, *Sci. Rep.* **2019**, 9, 10582.
- [45] K. Takada, H.-B. Sun, S. Kawata, *Appl. Phys. Lett.* **2005**, 86, 071122.
- [46] A. Schleunitz, V. A. Guzenko, M. Messerschmidt, H. Atasoy, R. Kirchner, H. Schiff, *Nano Converg.* **2014**, 1, 7.
- [47] N. Chidambaram, R. Kirchner, R. Fallica, L. Yu, M. Altana, H. Schiff, *Adv. Mater. Technol.* **2017**, 2, 1700018.
- [48] X. M. Zhao, Y. Xia, G. M. Whitesides, *Adv. Mater.* **1996**, 8, 837.
- [49] W. Jiang, H. Liu, Y. Ding, *Mater. Manuf. Processes* **2014**, 29, 59.
- [50] D. J. Carbaugh, S. Kaya, F. Rahman, *Mater. Res. Express* **2019**, 6, 045308.
- [51] F. Rahman, D. J. Carbaugh, J. T. Wright, P. Rajan, S. G. Pandya, S. Kaya, *Microelectron. Eng.* **2020**, 224, 111238.
- [52] E. H. Lee, G. R. Rao, L. K. Mansur, *Radiat. Phys. Chem.* **1999**, 55, 293.
- [53] S. Lewis, L. Piccirillo, *Advances in Diverse Industrial Applications of Nanocomposites*, InTechOpen, London, UK **2011**, pp. 475–500.
- [54] K. Balani, V. Verma, A. Agarwal, R. Narayan, *Biosurfaces: A Materials Science and Engineering Perspective*, **2014**, 329.
- [55] Z. Liu, J. Tam, O. Saeedi, D. X. Hammer, *Biomed. Opt. Express* **2018**, 9, 4246.
- [56] R. Davies, M. Kasper, *Annu. Rev. Astron. Astrophys.* **2012**, 50, 305.
- [57] S. A. Burns, A. E. Elsner, K. A. Sapoznik, R. L. Warner, T. J. Gast, *Prog. Retinal Eye Res.* **2019**, 68, 1.
- [58] M. Pircher, R. J. Zawadzki, *Biomed. Opt. Express* **2017**, 8, 2536.
- [59] J. F. De Boer, R. Leitgeb, M. Wojtkowski, *Biomed. Opt. Express* **2017**, 8, 3248.
- [60] C. Y. Santos, L. N. Johnson, S. E. Sinoff, E. K. Festa, W. C. Heindel, P. J. Snyder, *Alzheimer's and Dementia: Diagnosis, Assessment and Disease Monitoring* **2018**, 10, 196.
- [61] S. K. Wagner, D. J. Fu, L. Faes, X. Liu, J. Huemer, H. Khalid, D. Ferraz, E. Korot, C. Kelly, K. Balaskas, A. K. Denniston, P. A. Keane, *Transl. Vis. Sci. Technol.* **2020**, 9, 6.
- [62] P. Mécê, J. Scholler, K. Groux, C. Boccara, *Biomed. Opt. Express* **2020**, 11, 492.
- [63] O. M. Young, X. Xu, S. Sarker, R. D. Sochol, *Lab Chip* **2024**, 24, 2371.
- [64] A. T. Alsharhan, O. M. Young, X. Xu, A. J. Stair, R. D. Sochol, *J. Micromech. Microeng.* **2021**, 31, 044001.
- [65] G. L. Smith, A. S. Gesell, M. Restaino, J. B. Tyler, X. Xu, R. D. Sochol, S. Bergbreiter, N. Lazarus, *Adv. Mater. Technol.* **2024**, 9, 2301980.
- [66] H. Horng, K. O'Brien, A. Lamont, R. D. Sochol, T. J. Pfefer, Y. Chen, *Opt. Lett.* **2021**, 46, 1987.
- [67] Y. Fu, C. Lin, F. Y. Tsai, *Org. Electron.* **2009**, 10, 883.
- [68] Y. M. Sabry, M. Erfan, D. Khalil, T. Bourouina, *J. Opt. Microsyst.* **2022**, 2, 034001.
- [69] N. Jin, C. A. McLemore, D. Mason, J. P. Hendrie, Y. Luo, M. L. Kelleher, P. Kharel, F. Quinlan, S. A. Diddams, P. T. Rakich, *Optica* **2022**, 9, 965.